Principles and Instrumentation

1

Yutaka Yamashita and Masatsugu Niwayama

1.1 Light Absorption and Light Scattering

Quantification of chromophore concentration is based on the Beer-Lambert law [1–3]. In Fig. 1.1 the absorption coefficient μ_a is defined as

$$dI = -\mu_a \, I \, dl, \tag{1.1}$$

where dI is the change in intensity I of light moving along an infinitesimal path dl in a homogeneous medium. Integration over a thickness l (mm) yields

$$I_1 = I_0 \exp(-\mu_a \, l), \tag{1.2}$$

where I_0 is the incident light intensity. This equation is also expressed as base 10 logarithms as

$$I_l = I_0 \; 10^{-c\varepsilon l}. \tag{1.3}$$

Where c is the concentration of the compound, and ε is the molar absorption coefficient.

Transmission T is defined as the ratio of the transmitted light intensity to the incident light intensity, I_1/I_0. The optical density (OD) is given by

$$\mathrm{OD} = \log 10(1/T) = \log 10(I_0/I_1). \tag{1.4}$$

Y. Yamashita, BS
Central Research Laboratory, Hamamatsu Photonics KK, 5000 Hirakuchi,
Hamakita-ku, Hamamatsu City,
Shizuoka 434-8601, Japan
e-mail: yutaka@crl.hpk.co.jp

M. Niwayama, Ph.D. (✉)
Department of Electrical and Electronic Engineering, Shizuoka University,
3-5-1 Johoku, Nakaku, Hamamatsu, Shizuoka 432-8561, Japan
e-mail: tmniway@ipc.shizuoka.ac.jp

T. Jue and K. Masuda (eds.), *Application of Near Infrared Spectroscopy in Biomedicine*,
Handbook of Modern Biophysics 4, DOI 10.1007/978-1-4614-6252-1_1,

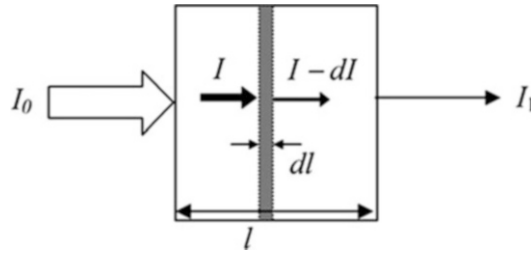

Fig. 1.1 Light transmission through a nonscattering medium

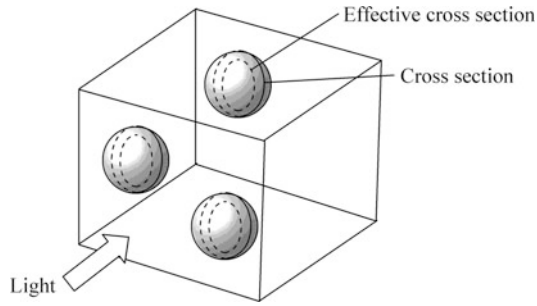

Fig. 1.2 Effective cross-section related to the scattering coefficient

When OD and ε are expressed as base 10 logarithms, the following expression is obtained from Eqs. 1.2, 1.3, and 1.4:

$$\mathrm{OD} = c\varepsilon l = \log_{10}(\mathrm{e})\ \mu_a l, \tag{1.5}$$

where $\log_{10}(\mathrm{e})$ is 0.43429.

Scattering of light in biological tissue is caused by refractive index mismatches at boundaries, such as cell membranes and organelles. The area that contributes to scattering is called the effective cross-section, as depicted in Fig. 1.2. The scattering coefficient μ_s (mm^{-1}) is expressed as the cross-sectional area (mm^2) per unit volume of the medium (mm^3). When the scattered photon does not return to the incident axis, μ_s can be defined as

$$I = I_0 \exp(-\mu_s l). \tag{1.6}$$

The scattering path length, defined as $1/\mu_s$, is the expected value of distance that a photon travels between scattering events and defines the distance that reduces incident light I_0 to I_0/e due to scattering. The total attenuation coefficient, μ_t is defined as the sum of the absorption and scattering coefficients, and $1/\mu_t$ is called the mean free path. When a photon is incident along the direction **i**, the angular probability of the photon being scattered in the direction **s** is given by the phase function f(**i**,**s**). The phase function is conventionally expressed as a function of the cosine of the scattering angle. The anisotropy can be represented as the mean cosine of the scattering angle, and the anisotropy factor g is defined as

$$g = \int_{-1}^{1} \cos\theta\, f(\cos\theta) d\cos\theta. \tag{1.7}$$

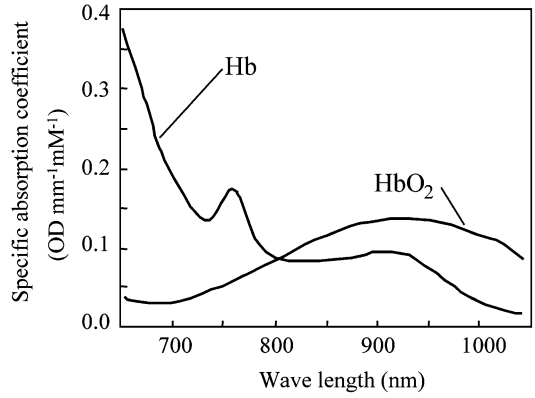

Fig. 1.3 Absorption spectra of oxyhemoglobin and deoxyhemoglobin

When $g = 0$ scattering is isotropic. Moreover, when $g = 1$ the incident light travels in a straight line. In contrast, when $g = -1$ complete backward scattering is observed. Biological tissues arestrongly forward-scattering media ($0.69 < g < 0.99$). The reduced scattering coefficient (μ'_s) is defined using the anisotropy factor as follows:

$$\mu'_s = \mu_s(1 - g). \tag{1.8}$$

The reduced scattering coefficient can be interpreted as representing the equivalent isotropic scattering coefficient and is used for the diffusion theory or Monte Carlo simulation when assuming isotropic scattering.

1.2 Optical Properties of Tissue

Hemoglobin is an iron-containing protein in red blood cells. One mole of deoxygenated hemoglobin (Hb) binds with four moles of oxygen to become oxygenated hemoglobin (HbO_2). The absorption spectra of oxygenated hemoglobin and deoxygenated hemoglobin [4] are shown in Fig. 1.3. The curves of the two hemoglobins intersect at about 800 nm, and the crossing point is called the isosbestic point. Since myoglobin and hemoglobin have similar absorption spectra, it is not easy to distinguish concentrations with spectroscopy. The separation of absorbers is also described in §1.4.

The absorption coefficient for water [5] is shown in Fig. 1.4. The absorption of water is small at wavelengths between about 200 and about 900 nm. Considering all components related to absorption in biological tissues, measurements at wavelengths between 680 and 950 nm are particularly suitable for spectroscopy.

Although many values for the optical properties of muscle and the overlying tissues (fat and skin) have been reported, there are significant differences in the results depending on the method of tissue preparation (fresh, saline-immersed, frozen, or thawed) and the theoretical analysis (diffusion theory, adding–doubling, Monte Carlo lookup tables). In Table 1.1 the optical properties of muscle, fat, dermis, and epidermis at wavelengths between 630 and 850 nm are given.

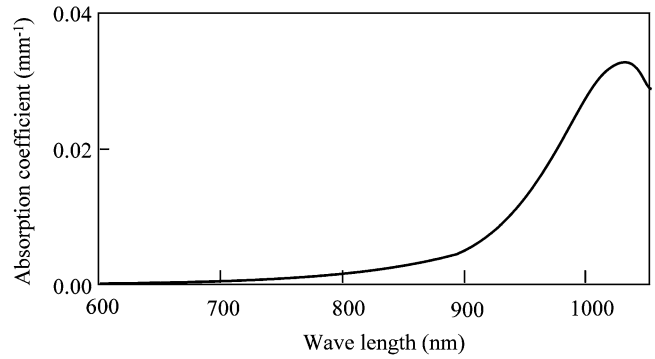

Fig. 1.4 Absorption spectrum of water

Table 1.1 Optical properties of muscle, fat, bone, dermis, and epidermis

Sample	λ (nm)	μ_a (mm^{-1})	μ_s' (mm^{-1})	References
Muscle				
Human forearm (in vivo)	800	0.015	1.0	Ferrari [6]
Human forearm (in vivo)	825	0.021–0.027	0.45–0.87	Zaccanti [7]
Human calf (in vivo)	825	0.018–0.028	0.51–0.85	Zaccanti [7]
Bovine muscle (in vitro)	633	0.096	0.53	Kienle [8]
Bovine muscle (in vitro)	751	0.037	0.34	Kienle [8]
Human calf (in vivo)	800	0.017 ± 0.005	0.80–1.1	Matcher [9]
Fat				
Human mamma (in vivo)	800	0.0017–0.0032	0.72–1.22	Mitic [10]
Human mamma (in vivo)	800	0.0023–0.0026	0.80–1.1	Suzuki [11]
Bovine fat (in vitro)	751	0.0021	1.0	Kienle [8]
Bone				
Pig skull (in vitro)	650	0.05	2.6	Firbank [12]
Pig skull (in vitro)	960	0.04	1.32	Firbank [12]
Human skull (in vivo)	849	0.022	0.91	Bevilacqua [13]
Dermis				
Pig dermis (in vitro)	790	0.018	1.4	Beek [14]
Pig dermis (in vitro)	850	0.033	0.9	Beek [14]
Epidermis				
Pig epidermis (in vitro)	790	0.24	1.9	Beek [14]
Pig epidermis (in vitro)	850	0.16	1.4	Beek [14]

1.3 Near-Infrared Spectroscopy

Spectroscopic measurement of in vivo tissue was first studied by Nicolai et al. [15] in 1932. They examined the optical characteristics of hemoglobin. The first practical ear oximeter for aviation use was developed by Millikan [16] ten years later. In 1949 Wood and Geraci [17] modified this instrument to obtain absolute values of oxygen saturation of arterial blood. The basic idea of this instrument was used to manufacture ear oximeters that were used in clinical settings until the 1970s. However, they did not have sufficient measurement stability for continuous monitoring of oxygen saturation because the calibration procedures were based on various extraneous assumptions. In 1974 Aoyagi et al. [18] presented a new idea called pulse oximetry, which utilizes the pulsation of arteries. This allowed for accurate measurement of oxygen saturation of arterial blood without the influence of

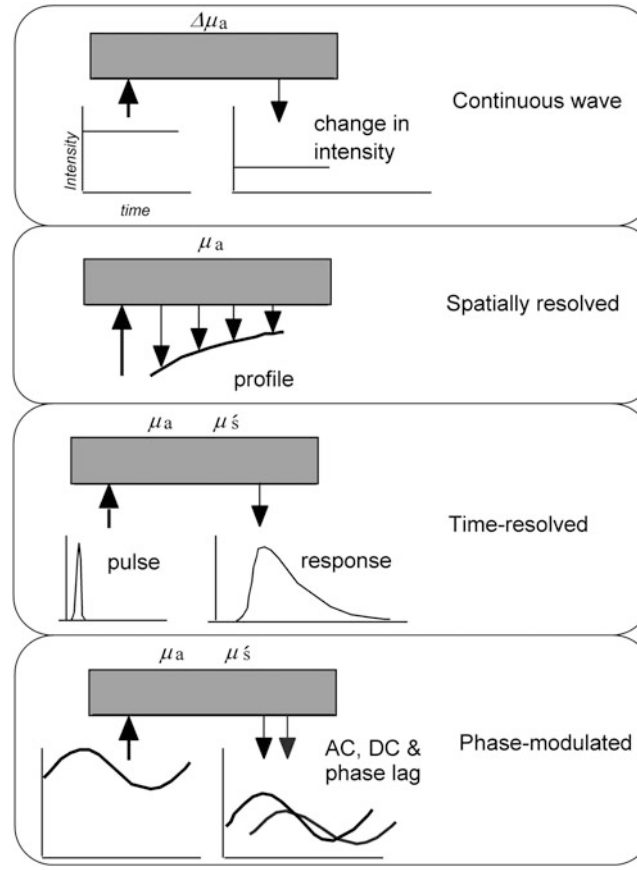

Fig. 1.5 Various techniques used in tissue oximetry employing NIRS

factors other than arterial blood. Pulse oximetry is now used in clinical medicine throughout the world. As mentioned above, oxygen saturation of arterial blood mainly reflects gas exchange occurring in the lungs and is an important factor for respiratory care. However, from the viewpoint of metabolism in tissues, measurement of blood oxygenation within the capillaries of each tissue is desirable.

In 1977, utilizing the relatively high penetration of near-infrared light, Jöbsis demonstrated that it was possible to measure attenuation spectra across the head of a cat, thereby obtaining information about tissue oxygenation [19]. In near-infrared spectroscopy (NIRS), tissue oxygenation is determined by analyzing the reflected or transmitted light intensity. However, NIRS using transmitted light is not suitable for clinical measurement, because it is difficult to detect transmitted light in adult human tissues; thus, reflection techniques are most commonly used nowadays. Several clinical studies on NIRS were conducted during the 1980s, including those by Ferrari et al. [20], Brazy et al. [21], Chance et al. [22], and Tamura et al. [23]. They detected changes in concentrations of oxy- and deoxyhemoglobin and in the cytochrome c oxidase redox state. They also demonstrated that NIRS is a useful, noninvasive technique for rapid detection of changes in tissue oxygenation.

Four major experimental techniques exist in the field of NIR spectroscopy, as shown in Fig. 1.5. The simplest one is continuous-wave spectroscopy (CWS) in which light of constant intensity is injected into tissue, and then the attenuated light signal is measured at a distance from the light source. The CWS technique has the limitation of obtaining only changes in optical density. More elaborate approaches are

Table 1.2 Advantages and disadvantages of CWS, SRS, TRS, and PMS

Parameters	CWS	SRS	TRS	PMS
[HbO_2], [Hb], [tHb]	Changes	Absolute value	**Absolute value**	**Absolute value**
		(Assumed μ_s')*		
SO_2	No	**Yes**	**Yes**	**Yes**
Absorption coefficient	No	**Yes**	**Yes**	**Yes**
		(Assumed μ_s')[a]		
Scattering coefficient	No	No	**Yes**	**Yes**
Time-resolved profile	No	No	**Yes**	No
Mean path length	No	No	**Yes**	**Yes**
Sampling rate (Hz)	≤**100**	≤**100**	≤1	≤10
Portability	**Wearable**/portable	**Wearable**/portable	Portable	Portable
Instrument cost	**Low**/moderate	**Low**/moderate	High	Moderate
Initial stabilization	**Not required**	**Not required**	Required	**Not required**
Light source	LED/laser diode	LED/laser diode	Laser diode	Laser diode
Detector	Silicon photodiode	Silicon photodiode	Photomultiplier tube	Avalanche photodiode

Underlined character = advantage, Bold character = important advantage, LED = light emitting diode. [a] = the calculation is possible in principle, but whether the parameter is calculated or not depends on the instrumentation

spatially resolved spectroscopy (SRS), time-resolved spectroscopy (TRS), and phase-modulated spectroscopy (PMS). Table 1.2 shows the advantages and disadvantages of the four measurement methods. The principles of these techniques are described in the following section.

1.4 Continuous-Wave NIRS

In NIRS, scattered light is detected at a distance from the light source, and tissue oxygenation is determined from the change in absorption coefficients of a tissue using the basic equations of conventional oximetry. Oximetry is the colorimetric measurement of the degree of oxygen saturation. Assuming that changes in light absorption are mainly due to changes in blood oxygenation or volume, [HbO_2] and [Hb] can be determined as follows. Change in the absorption coefficient of a tissue $\Delta\mu_a$ is expressed as

$$\Delta\mu_a = \varepsilon_\lambda^{HbO_2}\Delta[HbO_2] + \varepsilon_\lambda^{Hb}\Delta[Hb] \tag{1.9}$$

where $\varepsilon_\lambda^{HbO_2}$ and ε_λ^{Hb} are molar absorption coefficients of HbO_2 and Hb at wavelength λ, respectively. For example, ε_λ^{Hb} at a wavelength of 760 nm is 0.1674 OD mM^{-1} mm^{-1}, as reported by Matcher et al. [4]. In the above equations, ε_λ^{Hb} of 0.385 mM^{-1} mm^{-1} (= 0.1674 × ln10) is used because Matcher et al. defined OD as the logarithm to base 10 and μ_a is defined in base e. The two unknowns, $\Delta[HbO_2]$ and Δ[Hb], are obtained from measurements at two wavelengths. The NIRS instruments usually use a combination of wavelengths between 680 and 950 nm. These wavelengths are usually chosen to be around an isosbestic point (805 nm) of HbO_2 and Hb – for example, 770/830, 760/840, and 690/900 nm. When the difference of two wavelengths is large, changes in intensity due to wavelength

are easily obtained, but the change in optical path length would not be ignored. The following equations are solved on assumption that the path lengths of each wavelength are same:

$$\Delta[\mathrm{HbO_2}] = \frac{1}{k}\left(\varepsilon_2^{\mathrm{Hb}}\Delta\mu_{\mathrm{a1}} - \varepsilon_1^{\mathrm{Hb}}\Delta\mu_{\mathrm{a2}}\right), \tag{1.10}$$

$$\Delta[\mathrm{Hb}] = \frac{-1}{k}\left(\varepsilon_2^{\mathrm{HbO_2}}\Delta\mu_{\mathrm{a1}} - \varepsilon_1^{\mathrm{HbO_2}}\Delta\mu_{\mathrm{a2}}\right), \tag{1.11}$$

$$k = \varepsilon_1^{\mathrm{HbO_2}}\varepsilon_2^{\mathrm{Hb}} - \varepsilon_1^{\mathrm{Hb}}\varepsilon_2^{\mathrm{HbO_2}}. \tag{1.12}$$

The change in absorption, $\Delta\mu_a$, can be determined by various NIRS techniques, such as CWS, SRS, PMS, and TRS. The CWS method, which is the simplest one, only enables determination of change in absorption. In contrast, the optical properties in absolute values can be obtained by using SRS, PMS, or TRS. However, with any technique it is difficult to quantify the concentration other than that of hemoglobin, such as myoglobinin muscle tissue, cytochrome oxidase, carboxy-hemoglobin, and methemoglobin. Schenkman et al. [24, 25] reported a method for quantification of myoglobin and hemoglobin using the difference in peak position around 760 nm at near-infrared wavelengths. A composite myoglobin–hemoglobin peak would be slightly shifted by the absorption of hemoglobin derivatives and path length for each wavelength. Alternatively, some researchers have used NMR to observe the distinct Mb and Hb signals and then apply the results to determine Mb and Hb contributions in the NIRS spectra [26, 27].

Further studies with accurate quantification of small-quantity absorbers, mentioned above, scattering coefficient (or path length) for each wavelength, and combination of spectroscopic techniques could potentially form a basis for developing key technologies to measure the myoglobin and hemoglobin contribution to the NIRS signal.

In CW-NIRS, change in the optical density – defined by $\Delta\mathrm{OD} = \ln(R_0/R)$, where R_0 and R are intensities of backscattered light at a reference state (usually taken at the start of measurement) and during measurement, respectively – is measured. Assuming that the scattering coefficient does not change during measurement, we can determine $\Delta\mu_a$ using the modified Beer–Lambert law: $\Delta\mathrm{OD} = \Delta\mu_a d$, where $d = \partial\mathrm{OD}/\partial\mu_a$, which is defined as the differential path length and is equal to the mean optical path length.

CW-NIRS systems measure only ΔOD, and at least two different wavelengths are usually employed to obtain spectral information. Relative changes of $\mathrm{HbO_2}$ and Hb are continuously monitored utilizing Eqs. 1.10 and 1.11. The CW method is advantageous because it is highly sensitive, enabling a data sampling rate of less than a second, economical, and can be miniaturized to the extent of a multipoint monitor even for imaging. The assembly of a multiwavelength, multisource, multidetector imager for brain function and the circuit diagram are depicted in Fig. 1.6 [28].

Silicon photodiodes and multiwavelength light-emitting diodes (LEDs) are used as detectors and the near-infrared light source, respectively. They are held by elastic bands at a source–detector distance of 3 cm. The penetration depth of light and the spatial resolution are about 1.5 and 2 cm, respectively. Because digital gain control is used, the system can readily be controlled over a 20-dB range to equalize 16-channel signals. The output is then connected to a multiplexer (MUX) switch, which is synchronized with the flashing of the LED, so that one wavelength is sampled by separate integrating capacitors, which gives an RC charging time constant. The stored signal in this capacitor can be updated step by step by using the MUX switch. The storage capacitor is then oversampled by an analog-to-digital converter (ADC) at 250 samples/s to avoid aliasing. The temporal resolution of oxygenation measurement is $\geq$0.3 s.

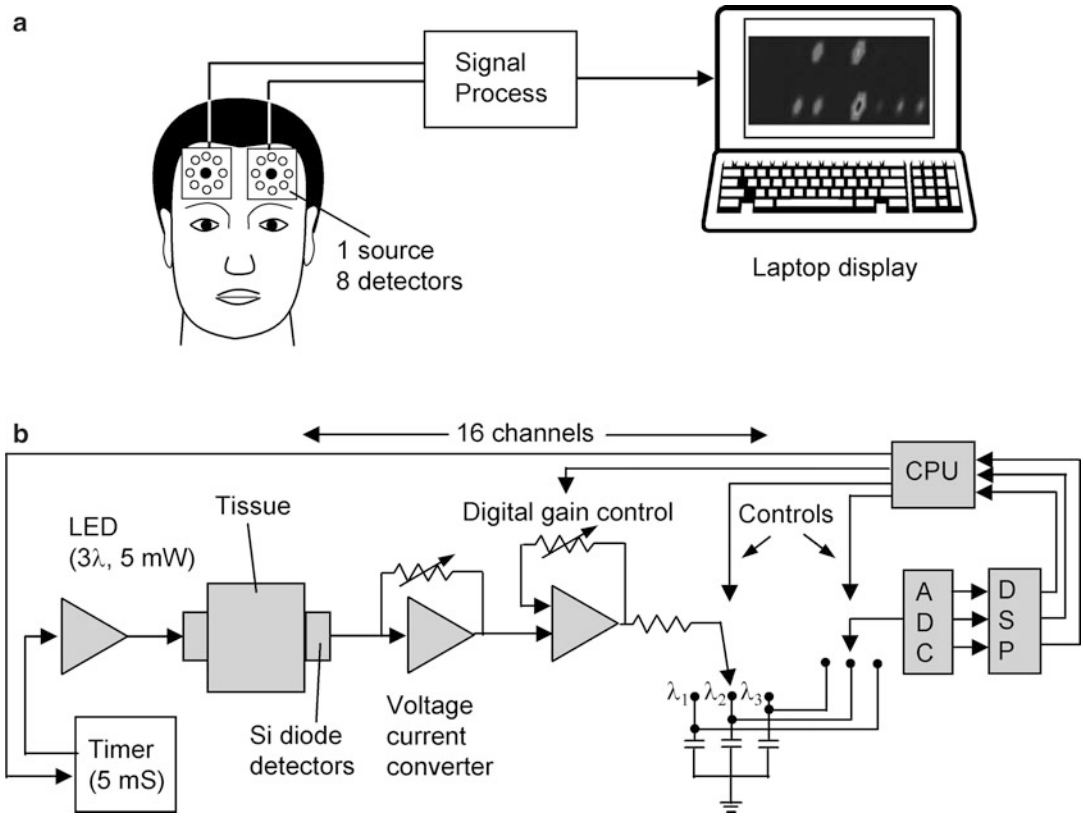

Fig. 1.6 The 16-channel "CW imager" is illustrated in (**a**) giving circuit constants and component values for one channel in (**b**)

Brain activation was monitored during the anagram test, which required the subject to identify a five-letter word from some items. The imager pad is centered on the nose bridge and symmetrically attached to the forehead, eyebrow to hairline, and temple to temple. The covering area is corresponding to Brodmann's areas 9 and 10, which are the part of the frontal cortex in the human brain. The subject's signals are illustrated in Fig. 1.7. The data show postsolution hyperemia and brief deoxygenation prior to problem solving and prolonged hyperoxygenation thereafter.

Although the CW method gives only relative values, it is sufficient for many cases, such as studies of the functional activity of the brain [29–32] or interventional studies for testing reactions on drugs or changes in treatment.

1.5 Spatially Resolved NIRS

Patterson et al. [33] proposed that the effective attenuation coefficient μ_{eff} of tissues can be obtained by measuring the spatial profile of the intensity of backscattered light as a function of the distance from the light source using a large source–detector separation. They showed that the intensity of reflected light R can be expressed as follows:

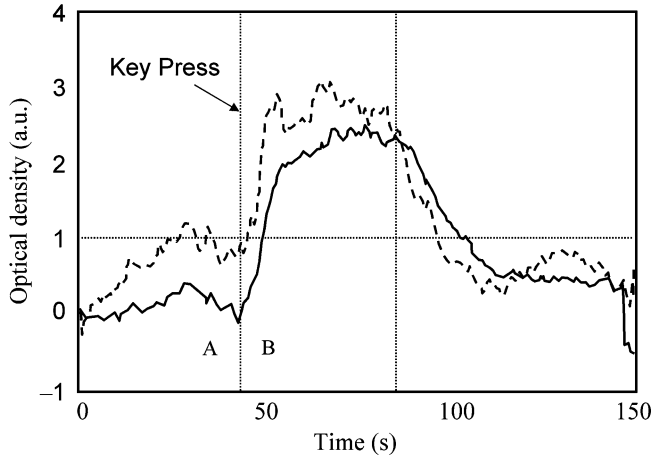

Fig. 1.7 Raw waveform data obtained during an anagram test. *Dashed line*: blood volume; *solid line*: oxygenation. The decision that the anagram has been solved is indicated by the *dashed vertical line* labeled "Key press"

$$R \propto \frac{\exp(-\mu_{\text{eff}})}{\rho^2}, \tag{1.13}$$

where $\mu_{\text{eff}} = \sqrt{3\mu_{\text{a}}(\mu_{\text{a}} + \mu'_{\text{s}})}$.

In the case of CW spectroscopy, the local reflectance $I(\rho)$ at position ρ is expressed as an integral of $R(\rho, t)$ over time, and OD is defined as the negative of the logarithm of $I(\rho)$.

Thus, OD is expressed by

$$\begin{aligned} OD &= -\ln I(\rho) \\ &= -\ln(z_0/2\boldsymbol{\pi}) + \frac{3}{2}\ln\left(\rho^2 + {z_0}^2\right) - \ln\left(1 + \mu_{\text{eff}}\left(\rho^2 + {z_0}^2\right)^{1/2}\right) + \mu_{\text{eff}}\left(\rho^2 + {z_0}^2\right)^{1/2}. \end{aligned} \tag{1.14}$$

In the measurement of human tissues, if $\rho^2 \gg {z_0}^2$ is assumed, $\mu_{\text{eff}}\,\rho \gg 1$, the following equation is derived.

$$\text{OD} = -\ln(z_0/2\pi) + 3\ln(\rho) - \ln(\mu_{\text{eff}}\rho) + \mu_{\text{eff}}\rho. \tag{1.15}$$

Differentiating OD with respect to ρ and assuming that $\mu_{\text{a}} \ll \mu_{\text{s}}'$ yield the following relation [34, 35]:

$$\frac{\partial \text{OD}}{\partial \rho} = -\frac{\partial}{\partial \rho}\ln I(\rho) = \frac{2}{\rho} + \sqrt{3\mu_a \mu_s'},$$

$$\therefore \mu_a \mu_s' = \frac{1}{3}\left(\frac{\partial \text{OD}}{\partial \rho} - \frac{2}{\rho}\right)^2. \tag{1.16}$$

where $\partial \text{OD}/\partial\rho$ is the local gradient of attenuation with respect to the source–detector separation.

Fig. 1.8 Spatially resolved spectroscopy system (NIRO-200NX) with an optical probe consisting of photodiodes and a light source

In the first-order approximation, μ'_s can be assumed to be constant within a narrow wavelength region of NIR light. Then the relative concentration changes of HbO_2 and Hb are derived from the following equation:

$$\begin{bmatrix} \left(\frac{\partial \mathrm{OD}(\lambda_1)}{\partial \rho}\right)^2 - \frac{2}{\rho} \\ \left(\frac{\partial \mathrm{OD}(\lambda_2)}{\partial \rho}\right)^2 - \frac{2}{\rho} \\ \left(\frac{\partial \mathrm{OD}(\lambda_3)}{\partial \rho}\right)^2 - \frac{2}{\rho} \end{bmatrix} = 3\mu'_s \begin{bmatrix} \varepsilon_{\mathrm{HbO_2}}(\lambda_1) & \varepsilon_{\mathrm{Hb}}(\lambda_1) \\ \varepsilon_{\mathrm{HbO_2}}(\lambda_2) & \varepsilon_{\mathrm{Hb}}(\lambda_2) \\ \varepsilon_{\mathrm{HbO_2}}(\lambda_3) & \varepsilon_{\mathrm{Hb}}(\lambda_3) \end{bmatrix} \begin{bmatrix} C_{\mathrm{HbO_2}} \\ C_{\mathrm{Hb}} \end{bmatrix}. \tag{1.17}$$

Moreover, the tissue oxygenation index (TOI) is calculated using the following equation:

$$\mathrm{TOI} = \frac{C_{\mathrm{HbO_2}}}{C_{\mathrm{HbO_2}} + C_{\mathrm{Hb}}} \times 100\ (\%). \tag{1.18}$$

A commercially available instrument using SRS for the measurement of hemoglobin saturation has been developed by Hamamatu Photonics, as shown in Fig. 1.8 [35].

A NIRO 300 was incorporated into an established multimodal monitoring system, enabling recording of cerebral hemodynamic changes during carotid endarterectomy (CEA) [36]. Brief periods of cerebral ischemia often occur during cross-clamping of the internal carotid artery (ICA) during surgery. Multimodal monitoring consists of frontal cutaneous laser-Doppler flowmetry (LDF) and transcranial Doppler mean flow velocity (FV) measurements of the ipsilateral middle cerebral artery. Typical data obtained during CEA are shown in Fig. 1.9. Sequential clamping was performed on the external carotid artery (ECA) before ICA clamping. The measurements obtained by LDF can be seen to fall only when the ECA clamp is applied. In this case the drop in FV is seen to be specific to ICA clamping, similar to the drop in the TOI. On insertion of an ICA vascular shunt, FV, and TOI were restored to values approaching baseline levels.

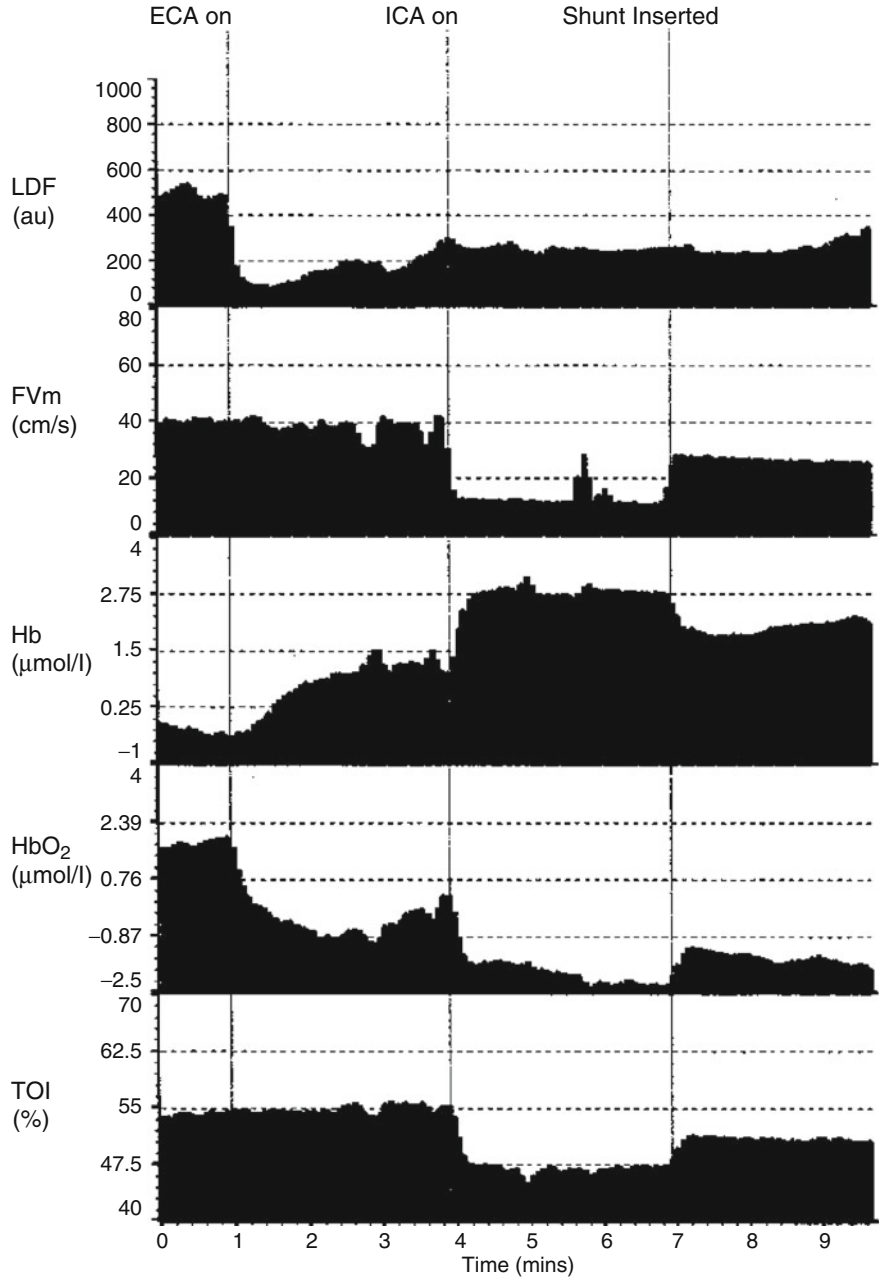

Fig. 1.9 Data obtained from a patient during elective carotid endarterectomy (CEA). *Vertical lines* demonstrate time of application of vascular clamps

1.6 Time-Resolved NIRS

In TRS temporal changes in the reflected light intensity are measured after irradiation of a picosecond pulse, thereby giving a distribution of the total path length of a photon traveling in the scattering medium [6, 37–39]. This technique can be used to determine the absorption coefficient and the

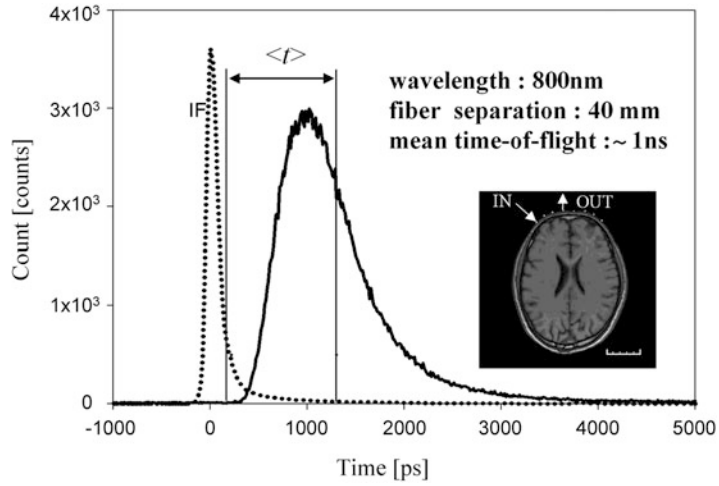

Fig. 1.10 Time-resolved waveform of the incident short pulse and reflectance at a 40-mm separation

reduced scattering coefficient of tissues. A method for determining the absorption and scattering coefficients is based on a curve fitting between measured data and a theoretical curve obtained by diffusion theory. When a semiinfinite medium is assumed and the zero-boundary condition is applied, the reflectance R at a source–detector separation ρ and time t is given [40] by

$$R(\rho,t) = (4\pi cD)^{-3/2}(\mu_a + \mu_s{}')^{-1}t^{-5/2}\exp\left(-\frac{\rho^2 + (\mu_a + \mu_s{}')^{-2}}{4cD}\frac{1}{t}\right)\exp(-\mu_a ct). \tag{1.19}$$

Taking the natural logarithm on both sides of Eq. 1.19 and assuming that $\rho \gg (\mu_a + \mu'_s)^{-1}$,we obtain the following equation:

$$\ln[R(\rho,t)] = \kappa - \frac{5}{2}\ln(t) - \left(ct + \frac{3\rho^2}{4ct}\right)\mu_a - \frac{3\rho^2}{4ct}\mu_s{}', \tag{1.20}$$

where $\kappa = -\ln(4\pi cD)3/2 - \ln(\mu_a + \mu_s{}')$. Simple mean least-squares-fitting algorithms can be used to determine μ_a and $\mu_s{}'$ from experimental data. A typical waveform of time-resolved measurement is shown in Fig. 1.10.

A TRS system (TRS-20) uses the time-correlated single-photon counting (TCPC) method to measure the temporal profile of the detected photons (see Fig. 1.11). The system [41] consists of a three-wavelength (759, 797, and 833 nm) light pulse source (PLP: Picosecond Light Pulser, Hamamatsu Photonics KK, Hamamatsu, Japan), which generates light pulses with a peak power of about 60 mW, pulse width of 100 ps, pulse rate of 5 MHz, and an average power of 30 μW for one wavelength. For the detection, a photomultiplier tube (PMT, H7422-50MOD, Hamamatsu Photonics KK) was used in photon-counting mode. The timing signals were received and accumulated by a TRS circuit that consists of a constant-fraction discriminator, a time-to-amplitude converter, an ADC, and histogram memory. The PLP emits three-wavelength light pulses in turn, and the light pulses are guided into one illuminating optical fiber by a fiber coupler (CH20G-D3-CF, Mitsubishi Gas Chemical Company Inc., Japan). A single optical fiber (GC200/250L, FUJIKURA Ltd., Japan) with a numerical aperture (NA) of 0.21 and a core diameter of 200 μm was used for illumination.

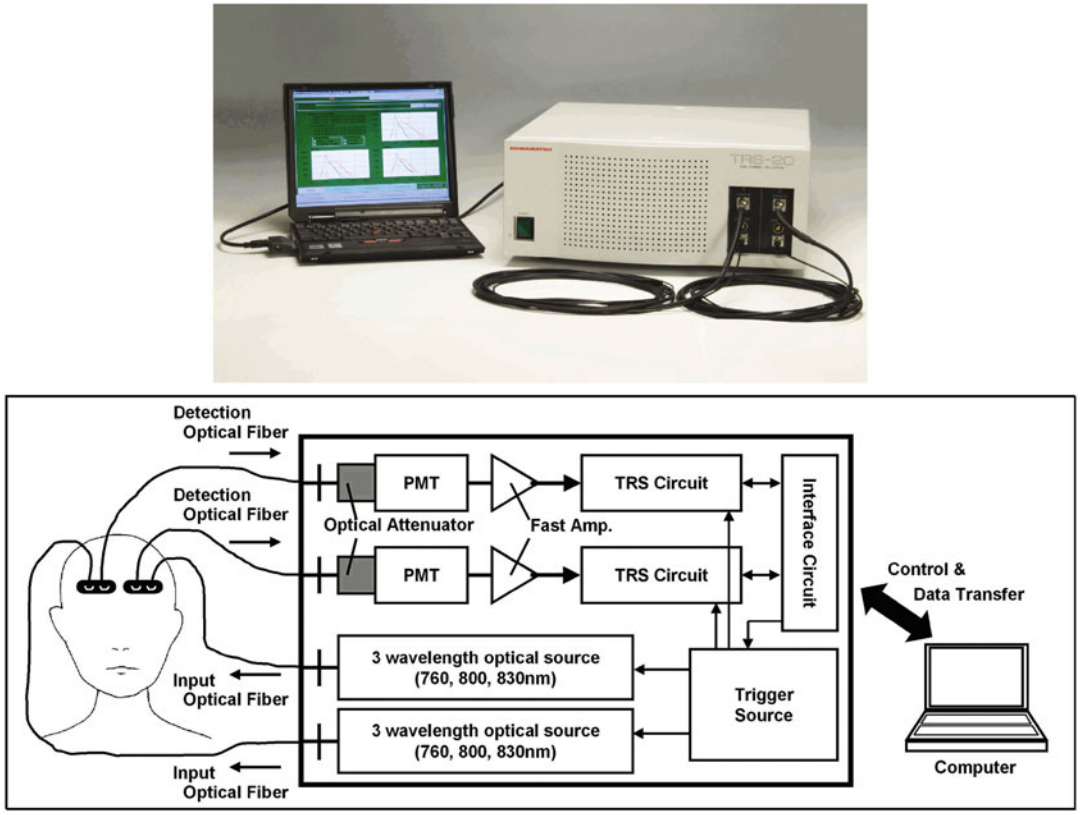

Fig. 1.11 Schematic diagram of a time-resolved spectroscopy system

An optical bundle fiber (LB21E, Moritex Corp., Japan) with an NA of 0.21 and a bundle diameter of 3 mm was used to collect diffuse light from the tissues. TRS-20 has two sets of PLP and TCPC detectors, enabling the independent measurement of two portions.

TRS allows for determination of relative light intensity, mean optical path length, transport scattering coefficient (μ'_s), and μ_a. The intensity can be obtained by integrating the temporal profiles, and the modified Beer–Lambert law uses this information to calculate absorbance changes. The mean optical path lengths were calculated from the center of gravity of the temporal profile [42]. The calculations of the intensity, absorbance change, and mean path length are model independent. Applying the diffusion equation for semiinfinite homogeneous media with zero-boundary conditions in reflectance mode into all observed temporal profiles, we obtained the values of μ'_s and μ_a using the nonlinear least-squares method [43].

If it is assumed that absorption in the 700–900 nm range arises from absorption of HbO_2, Hb, and water, $\mu_{a\lambda}$ of the measured wavelengths: λ (759, 797, and 833 nm) is expressed as shown in simultaneous Eq. 1.21 [44, 45]:

$$\begin{aligned}
\mu_{a759nm} &= \varepsilon_{HbO_2 759nm} C_{HbO_2} + \varepsilon_{Hb759nm} C_{Hb} + \mu_{aH_2O759nm} \\
\mu_{a797nm} &= \varepsilon_{HbO_2 797nm} C_{HbO_2} + \varepsilon_{Hb797nm} C_{Hb} + \mu_{aH_2O797nm} \\
\mu_{a833nm} &= \varepsilon_{HbO_2 833nm} C_{HbO_2} + \varepsilon_{Hb833nm} C_{Hb} + \mu_{aH_2O833nm},
\end{aligned} \tag{1.21}$$

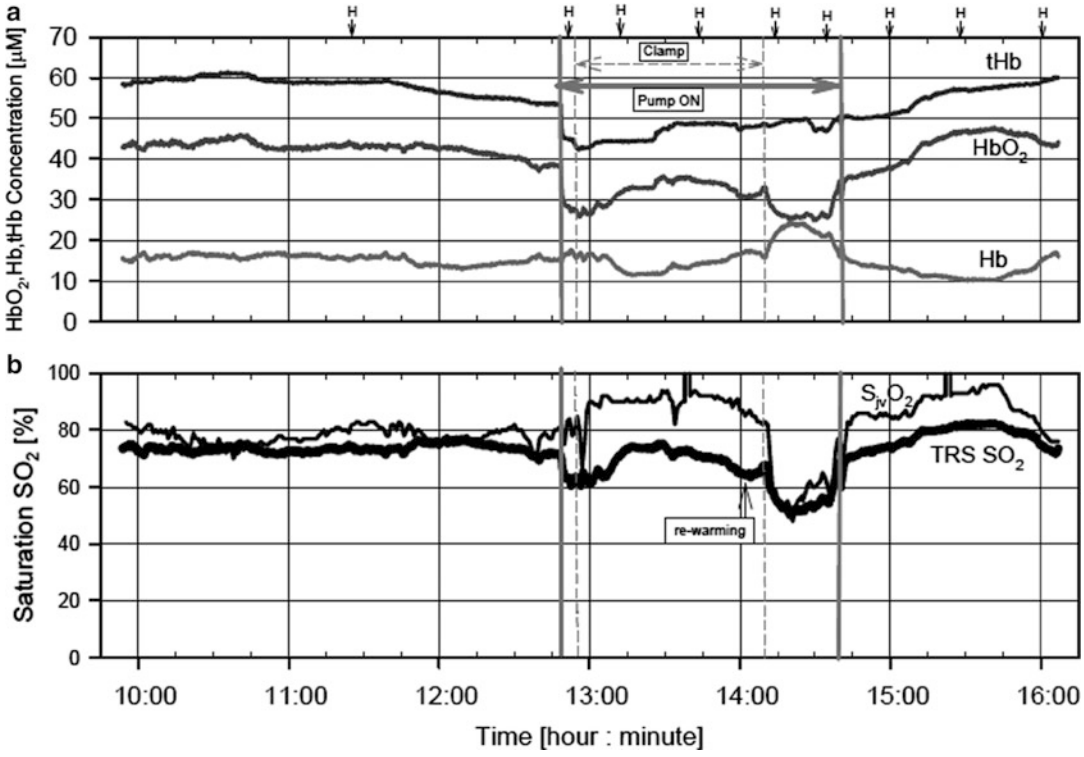

Fig. 1.12 Fluctuations of SO_2 and $SjvO_2$ were separated during extracorporeal circulation in one patient

where $\varepsilon_{m\lambda}$ is the molar absorption coefficient of substance m at wavelength λ, and C_m is the concentration of substance m. After subtracting water absorption from μ_a at each wavelength, assuming that the volume fraction of the water content was constant, $[HbO_2]$ and [Hb] were determined using the least-squares-fitting method.

The total concentrations of Hb (tHb) and tissue oxygen saturation (SO_2) were calculated as follows:

$$\mathrm{tHb} = \mathrm{Hb}_{\mathrm{O}_2} + \mathrm{Hb}, \tag{1.22}$$

$$\mathrm{SO}_2 = \frac{[\mathrm{HbO}_2]}{[\mathrm{tHb}]} \times 100. \tag{1.23}$$

The hemodynamics of the brain were monitored by TRS during a coronary artery bypass grafting surgery using an artificial heart-and-lung machine [45]. Figure 1.12 shows the time course of changes in $[HbO_2]$, [Hb], and [tHB] in (A) and SO_2 and the internal jugular vein oxygen saturation ($SjvO_2$) in (B). When extracorporeal circulation was started by the pump, HbO_2 and tHb decreased rapidly. At the end of extracorporeal circulation, those values returned to the initial levels. SO_2 estimated by TRS was found to be nearly the same as $SjvO_2$ before and after extracorporeal circulation, but during circulation they behaved differently in this case.

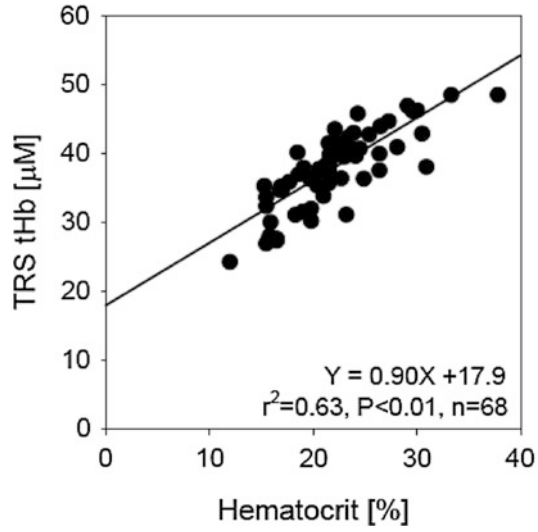

Fig. 1.13 Relationship between tHb by TRS-10 and hematocrit (Hct) in nine patients

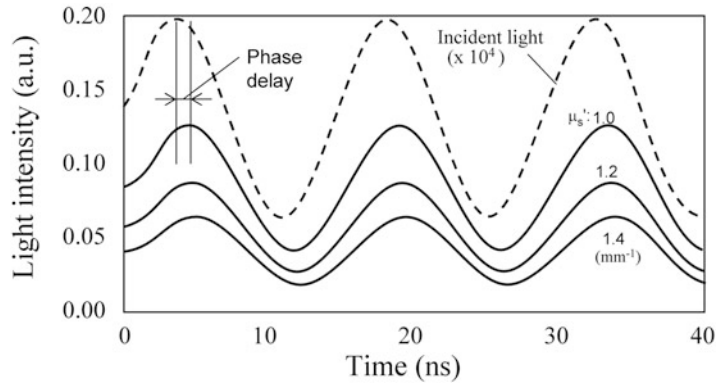

Fig. 1.14 Phase shift between the incident light (*dashed line*) and scattered light through tissues (*solid lines*) at 70 MHz of modulation frequency

Figure 1.13 shows the correlation between the hematocrit (Hct) values of arterial blood and tHb in 9 patients. The correlation among patients was high ($r^2 = 0.63$), showing that tHb measured by TRS has good linearity with Hct.

1.7 Phase-Modulated NIRS

Phase-modulated (frequency domain) measurements were first reported by Chance in 1949 [46]. Pulse code or phase modulation gives mean time delay between source and detector. The time delay is related to light scattering and absorption, including biological signals. Figure 1.14 shows an example of the phase shift obtained by a computer simulation. Different types of equipment were developed

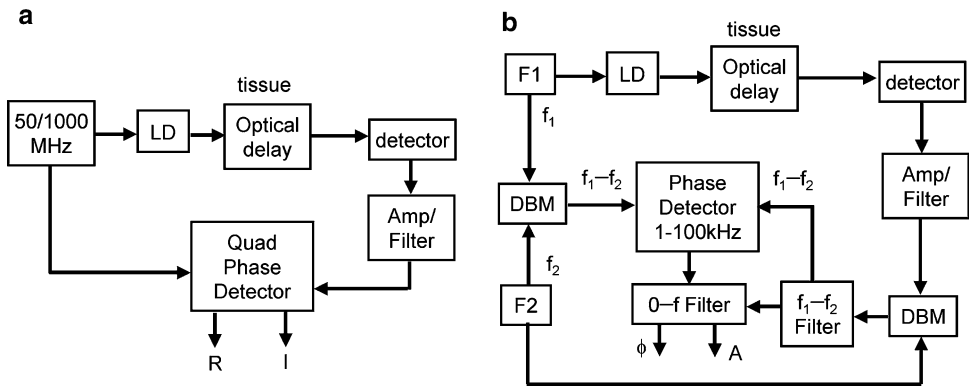

Fig. 1.15 Schematic diagram of phase-modulated homodyne (**a**) and heterodyne (**b**) NIRS systems

and classified by the multiplicity of wavelengths and the type of phase detection. Homodyne systems [47], heterodyne systems [48, 49], and network analyzers [50] were used for measuring the phase (see Fig. 1.15). The performance of both homodyne and heterodyne detection systems was examined, and it was suggested that a homodyne system has advantages in terms of simplicity of construction and execution, while a heterodyne system has high precision and the possibility of low-frequency phase detection [51].

The supporting theoretical background is the diffusion equation. An analytical solution was obtained on the basis of an assumption that the modulation frequency ($\omega/2\pi$) is much smaller than the typical frequency of scattering processes (i.e., $c\mu'_s$, where c is the speed of light in a medium). The condition for this assumption is satisfied by most biological tissues in an NIR spectral region for modulation frequencies up to 1 GHz. Fishkin and Gratton obtained the following expressions [52]:

$$\ln(\rho U_{\mathrm{dc}}) = -\rho\sqrt{\frac{\mu_{\mathrm{a}}}{D}} + \ln\left(\frac{S}{4\pi D}\right), \tag{1.24}$$

$$\ln(\rho U_{\mathrm{ac}}) = -\rho A\cos\left(\frac{\theta}{2}\right) + \ln\left(\frac{kS}{4\pi D}\right), \tag{1.25}$$

$$\phi = \rho A\sin\frac{\theta}{2}, \tag{1.26}$$

$$\theta = \tan^{-1}\left(\frac{\omega}{\mu_{\mathrm{a}}c}\right),\quad A = \left(\frac{\mu_{\mathrm{a}}^2c^2+\omega^2}{c^2D^2}\right)^{1/4}, \tag{1.27}$$

where ϕ is the phase shift of a detected signal relative to an excited signal, U_{dc} is the direct current (dc) component of the photon density, U_{ac} is the amplitude of the alternating current (ac) component of the photon density, S is the source strength (in photons per second), and k is defined as the ratio of the ac to the dc components of the intensity. Fantini et al. [53] developed practical instrumentation based on diffusion theory with multidistance detection. As mentioned above, various phase-modulated NIRS systems have been developed. A typical commercial phase-modulated NIRS system is depicted in Fig. 1.16. OxiplexTS (ISS Inc., Champaign, IL) is a tissue oximeter that includes light sources (690 and 830 nm), with a multidistance emitter array, and one detection channel using PMT.

Fig. 1.16 Phase-modulated NIRS system, ISS Oxiplex (ISS Inc.)

The detection type is heterodyne with an offset frequency of several kHz at a 110-MHz modulation frequency. Various optical probes can be coupled to the system for specific medical research applications.

Problem

1.1. How can the weak photocurrent of an Si photodiode be converted to a voltage signal on continuous-wave NIRS or spatially resolved NIRS?

Further Reading

Demrow B (1971) Op amps as electrometers or — the world of fA. Anal Dial 5(2): 48–49
Frenzel LE (2007) Accurately measure nanoampere and picoampere currents. Electron Design Strat News, Feb 15
Hutchings MJ, Blake-Coleman BC (1994) A transimpedance converter for low-frequency, high-impedance measurements. Meas Sci Technol 5(3):310–313
Rako P (2007) Measuring nanoamperes. Electron Design Strat News, Apr 26

References

1. Bouguer P (1729) Essai d'optique sur la gradation de la lumière. Claude Jombert, Paris
2. Lambert JH (1760) Lambert's photometrie: photometria, sive de mensura et gradibus luminis, colorum et umbrae. Wilhelm Engelmann, Berlin
3. Beer A (1852) Bestimmung der absorption des rothen Lichts in farbigen Flüssigkeiten. Annu Rev Phys Chem 86:78–88
4. Matcher SJ, Elwell CE, Cooper CE, Cope M, Delpy DT (1995) Performance comparison of several published tissue near-infrared spectroscopy algorithms. Anal Biochem 227:54–68
5. Hale GM, Querry MR (1973) Optical constants of water in the 200-nm to 200-mm wavelength region. Appl Opt 12:555–563
6. Ferrari M, Wei Q, Carraresi L, De Blasi RA, Zaccanti G (1992) Time-resolved spectroscopy of the human forearm. J Photochem Photobiol B: Biol 16:141–153
7. Zaccanti G, Taddeucci A, Barilli M, Bruscaglioni P, Martelli F (1995) Optical properties of biological tissues. Proc SPIE 2389:513–521
8. Kienle A, Lilge L, Patterson MS, Hibst R, Steiner R, Wilson BC (1996) Spatially resolved absolute absorption coefficients of biological tissue. Appl Opt 35:2304–2314
9. Matcher SJ, Cope M, Delpy DT (1997) In vivo measurements of the wavelength dependence of tissue-scattering coefficients between 760 and 900 nm measured with time-resolved spectroscopy. Appl Opt 36:386–396

10. Mitic G, Közer J, Otto J, Plies E, Sökner G, Zinth W (1994) Time-gated transillumination of biological tissues and tissue like phantoms. Appl Opt 33:6699–6710
11. Suzuki K, Yamashita Y, Ohta K, Chance B (1994) Quantitative measurement of optical parameters in the breast using time-resolved spectroscopy phantom and preliminary in vivo results. Invest Radiol 29:410–414
12. Firbank M, Hiraoka M, Essenpreis M, Delpy DT (1993) Measurement of the optical properties of the skull in the wavelength range 650–950 nm. Phys Med Biol 38:503–510
13. Bevilacqua F, Piguet D, Marquet P, Gross JD, Tromberg BJ, Depeursinge C (1999) In vivo local determination of tissue optical properties: applications to human brain. Appl Opt 38:4939–4950
14. Beek JF, van Staveren HJ, Posthumus P, Sterenborg HJ, van Gemert MJ (1993) The influence of respiration on optical properties of piglet lung at 632.8 nm. Med Opt Tomogr 32:193–210
15. Nicolai L (1932) Über sichtbarmachung, verlauf und chemische kinetic der, oxyhemoglobinreduktion im lebendum gewebe, besonders in der menschlichen haut. Arch Gesch Physiol 229:372–384
16. Millikan GA (1942) The oximeter, an instrument for measuring continuously oxygen saturation of arterial blood in man. Rev Sci Instrum 13:434–444
17. Wood EH, Geraci JE (1949) Photoelectric determination of arterial oxygen saturation in man. J Lab Clin Invest 34:387–401
18. Aoyagi T, Kishi M, Yamaguchi K, Watanabe S (1974) Improvement of earpiece oximeter. Proc 13th Conf Jpn Soc Med Electron Biol Eng 12:90–91
19. Jöbsis FF (1977) Noninvasive, infrared monitoring of cerebral and myocardial oxygen sufficiency and circulatory parameters. Science 198:1264–1267
20. Ferrari M, Giannini I, Sideri G, Zanette E (1985) Continuous noninvasive monitoring of human brain by near infrared spectroscopy. Adv Exp Med Biol 191:873–882
21. Brazy JE, Lewis DV, Mitnick MH, Jöbsis FF (1985) Noninvasive monitoring of cerebral oxygenation in preterm infants. Pediatrics 75:217–225
22. Chance B, Nioka S, Kent J, McCully K, Fountai M, Greenfeld R, Holtom G (1988) Time-resolved spectroscopy of hemoglobin and myoglobin in resting and ischemic muscle. Anal Biochem 174:698–707
23. Tamura M, Hazeki O, Nioka S, Chance B, Smith DS (1988) The simultaneous measurements of tissue oxygen concentration and energy state by near-infrared and nuclear magnetic resonance spectroscopy. Adv Exp Med Biol 222:359–363
24. Schenkman KA, Marble DA, Feiglf EO, Burns DH (1999) Near-infrared spectroscopic measurement of myoglobin oxygen saturation in the presence of hemoglobin using partial least-squares analysis. Appl Spectrosc 53:325–331
25. Marcinek DJ, Amara CE, Matz K, Conley KE, Schenkman KA (2007) Wavelength shift analysis: a simple method to determine the contribution of hemoglobin and myoglobin to in vivo optical spectra. Appl Spectrosc 61:665–669
26. Tran TK, Sailasuta N, Kreutzer U, Hurd R, Chung Y, Mole P, Kuno S, Jue T (1999) Comparative analysis of NMR and NIRS measurements of intracellular PO_2 in human skeletal muscle. Am J Physiol 276:R1682–R1690
27. Xie H, Kreutzer U, Jue T (2009) Oximetry with the NMR signals of hemoglobin Val E11 and Tyr C7. Eur J Appl Physiol 107:325–333
28. Chance B, Nioka S, Zhao Z (2007) A wearable brain imager. IEEE Eng Med Biol 26:30–37
29. Hoshi Y, Tamura M (1993) Detection of dynamic changes in cerebral oxygenation coupled to neuronal function during mental work in man. Neurosci Lett 150:5–8
30. Chance B, Zhuang Z, UnAh C, Alter C, Lipton L (1993) Cognition-activated low-frequency modulation of light absorption in human brain. Proc Natl Acad Sci USA 90(8):3770–3774
31. Kato T, Kamei A, Takashima S, Ozaki T (1993) Human visual cortical function during photic stimulation monitoring by means of near-infrared spectroscopy. J Cereb Blood Flow Metab 13:516–520
32. Villringer A, Planck A, Hock C, Schleinkofer L, Dirnagl U (1993) Near infrared spectroscopy (NIRS): a new tool to study hemodynamic changes during activation of brain function in human adults. Neurosci Lett 154:101–104
33. Patterson MS, Schwartz E, Wilson BC (1989) Quantitative reflectance spectrophotometry for the noninvasive measurement of photosensitizer concentration in tissue during photodynamic therapy. Proc SPIE 1065:115–122
34. Matcher SJ, Kirkpatrick P, Nahid N, Cope M, Delpy DT (1995) Absolute quantification method in tissue near infrared spectroscopy. Proc SPIE 2389:486–495
35. Suzuki S, Takasaki S, Ozaki T, Kobayashi K (1999) A tissue oxygenation monitor using NIR spatially resolved spectroscopy. Proc SPIE 3597:582–592
36. Al-Rawi PJ, Smielewski P, Kirkpatrick PJ (2001) Evaluation of a near-infrared spectrometer (NIRO 300) for the detection of intracranial oxygenation changes in the adult head. Stroke 32:2492–2500
37. Chance B, Leigh JS, Miyake H, Smiths DS, Nioka S, Greenfeld R, Finander M, Kaufmann K, Levy W, Young M, Cohen P, Yoshioka H, Boretsky R (1988) Comparison of time-resolved and -unresolved measurements of deoxyhemoglobin in brain. Proc Natl Acad Sci USA 85:4971–4975
38. Delpy DT, Cope M, van der Zee P, Arridge S, Wray S, Wyatt JS (1988) Estimation of optical pathlength through tissue from direct time of flight measurement. Phys Med Biol 33(12):1433–1442

39. Nomura M, Hazeki O, Tamura M (1989) Exponential attenuation of light along the nonlinear optical path in the scattered media. Adv Exp Med Biol 248:71–80
40. Patterson MS, Chance B, Wilson BC (1989) Time resolved reflectance and transmittance for the noninvasive measurement of tissue optical properties. Appl Opt 28:2331–2336
41. Oda M, Yamashita Y, Nakano T, Suzuki A, Shimizu K, Hirano I, Shimomura F, Ohmae E, Suzuki T, Tsuchiya Y (2000) Nearinfrared time-resolved spectroscopy system for tissue oxygenation monitor. Proc SPIE 4160:204–210
42. Zhang H, Miwa M, Yamashita Y, Tsuchiya Y (1998) Simple subtraction method for determining the mean path length traveled by photons in turbid media. Jpn J Appl Phys 37–1(2):700–704
43. Ichiji S, Kusaka T, Isobe K, Okubo K, Kawada K, Namba M, Okada H, Nishida T, Imai T, Itoh S (2005) Developmental changes of optical properties in neonates determined by near-infrared time-resolved spectroscopy. Pediatr Res 58(3):568–572
44. Ohmae E, Ouchi Y, Oda M, Suzuki T, Yamashita Y (2006) Cerebral hemodynamics evaluation by near-infrared time-resolved spectroscopy: correlation with simultaneous positron emission tomography measurements. Neuroimage 29:697–705
45. Ohmae E, Oda M, Suzuki T, Yamashita Y, Kakihana Y, Matsunaga A, Kanmura Y, Tamura M (2007) Clinical evaluation of time-resolved spectroscopy by measuring cerebral hemodynamics during cardiopulmonary bypass surgery. J Biomed Opt 12(6):062112
46. Chance B, Hulsizer RI, MacNichol EF Jr, Williams FC (1949) Electronic time measurements, vol 20, MIT Radiation Laboratories Series. Boston Technical, Lexington
47. Ma HY, Du C, Chance B (1997) Homodyne frequency-domain instrument: I&Q Phase detection system. Proc SPIE 2979:826–837
48. Kohl M, Watson R, Cope M (1997) Optical properties of highly scattering media determined from changes in attenuation, phase and modulation depth. Proc SPIE 2979:365–374
49. Feddersen BA, Piston DW, Gratton E (1989) Digital parallel acquisition in frequency domain fluorometry. Rev Sci Instrum 60:2929–2936
50. Madsen SJ, Anderson ER, Haskell RC, Tromberg BJ (1994) Portable, high-bandwidth frequency-domain photon migration instrument for tissue spectroscopy. Opt Lett 19:1934–1936
51. Chance B, Cope M, Gratton E, Ramanujam N, Tromberg B (1998) Phase mesurement of light absorption and scatter in human tissue. Rev Sci Instrum 69:3457–3481
52. Fishkin JB, Gratton E (1993) Propagation of photon-density wave in strongly scattering media containing an absorbing semi-infinite plane bounded by a straight edge. J Opt Soc Am A 10:127–140
53. Fantini S, Franceschini MA, Maier J, Walker S, Barbieri B, Gratton E (1995) Frequency-domain multichannel optical detector for noninvasive tissue spectroscopy and oximetry. Opt Eng 34:32–42